nature geoscience

Article

https://doi.org/10.1038/s41561-024-01391-8

Diurnal warming rectification in the tropical Pacific linked to sea surface temperature front

Received: 9 October 2022

Accepted: 2 February 2024

Published online: 25 March 2024

Check for updates

Meghan F. Cronin[1] ✉, Dongxiao Zhang[1,2], Samantha M. Wills[1,2], J. E. Jack Reeves Eyre[3,4], LuAnne Thompson[5] & Nathan Anderson[1,2]

Sharp and rapid changes in the sea surface temperature (SST) associated with fronts and the diurnal cycle can drive changes in the atmospheric boundary-layer stability and circulation. Here we show how a one-dimensional surface ocean model forced with either high-resolution or daily averaged surface fluxes can be used to distinguish diurnal versus frontal SST anomalies observed from an uncrewed surface vehicle. The model, forced with daily satellite fluxes, shows that the diurnal warming is largest within the equatorial Pacific cold tongue of SST. The strong persistent SST front north of the cold tongue is evident in both the oceanic and atmospheric boundary-layer stability scales and, as a consequence, in the magnitude of the diurnal ocean warming. Using SST, barometric pressure and surface wind measurements from moorings at 0°, 95° W and 2° N, 95° W, we show that the front in the SST diurnal warming results in a weakened SST front in the afternoon and a corresponding reduced meridional gradient in the barometric pressure that appears to contribute to a diurnal pulsing of the surface meridional winds. To the extent that these modulate the surface branch of the Hadley cell, these diurnal variations may have remote impacts.

Surface wind observations[1] showing cuspy patterns clearly linked to oceanic tropical instability waves (TIWs) demonstrated conclusively that the ocean could force the atmosphere. In the two decades since this seminal study[1], there have been numerous investigations of atmospheric response to sea surface temperature (SST) fronts on a range of scales throughout the global oceans[2–5], with a lively debate about the mechanisms. Are the wind anomalies caused by the SST front's influence on atmospheric stability[6] or the SST front's impact on a barometric pressure gradient[7]? In a separate line of query, over the past several decades, there has been a growing recognition that the SST diurnal cycle can rectify into longer timescales, impacting air–sea fluxes of heat[8,9], momentum[10,11] and gas[12,13], which in turn can result in large-scale changes to the atmospheric hydrological cycle[14–17]. In this study, we step back and consider how SST fronts affect patterns of diurnal SST warming and how the SST diurnal cycle patterns potentially affect barometric pressure gradients and large-scale circulation.

When winds are weak and solar radiation is large, a diurnal warm layer can form[12] with maximum stratification in late afternoon that is subsequently eroded by night-time cooling and mixing. SST below the diurnal warm layer is referred to as the 'foundation' sea surface temperature (T_{fdn}). In late afternoon, when the diurnal layer is fully formed, T_{fdn} is found at 10 m or deeper. By contrast, at dawn, after the diurnal warm-layer stratification is completely removed, the foundation SST is the water temperature directly below the thermal skin layer[18].

[1]NOAA Pacific Marine Environmental Laboratory, Seattle, WA, USA. [2]Cooperative Institute for Climate, Ocean, and Ecosystem Studies (CICOES), University of Washington, Seattle, WA, USA. [3]Climate Prediction Center, NOAA National Center for Environmental Prediction, College Park, MD, USA. [4]ERT Inc., Laurel, MD, USA. [5]School of Oceanography, University of Washington, Seattle, WA, USA. ✉e-mail: Meghan.F.Cronin@noaa.gov

https://doi.org/10.1038/s41561-024-01391-8

Consequently, the bulk SST measured by an in situ sensor located a few centimetres to a few metres below the surface, $T(z_m)$, can have a large diurnal cycle, with a maximum in late afternoon and a minimum that is equivalent to T_{fdn} at dawn[12,19,20]. Throughout the diurnal cycle, the bulk SST differs from the ocean skin temperature (T_{skin}). The state-of-the-art Coupled Ocean–Atmosphere Response Experiment (COARE) bulk-flux algorithm[21–24] thus includes an option to extrapolate the measured bulk in situ SST to T_{skin} by estimating a warm-layer effect (ΔT_{warm}) and/or a cool-skin effect (ΔT_{cool}). The extrapolated skin temperature is then used to compute a more accurate estimate of air–sea fluxes.

In this Article, we show that the Fairall et al.[24] diurnal warm-layer model (Fig. 1) used in the COARE bulk-flux algorithm, hereinafter referred to as F96, can also be used to extrapolate the measured bulk SST to T_{fdn}. For SST and flux time series that cross fronts, extrapolation of the bulk SST to a T_{fdn} enables separation of SST anomalies due to diurnal warming from anomalies due to fronts. In addition, we show that F96 can be integrated for 24 hours to estimate the daily averaged warm effect from daily averaged surface fluxes if we add a parameterized wind gustiness to the daily averaged wind stress. This then allows us to use daily averaged satellite-based fluxes to examine the spatial patterns of the warm-layer effect that rectify into daily and longer timescales. In places, this rectification can be larger than the nominal cool-skin correction[25,26] of ~0.17 °C. Finally, the model helps explain a curious and consequential feature observed across the observing system[11,27], including from uncrewed surface vehicles (USVs), satellite-based products and moored buoy time series: the sharp SST front in the eastern equatorial Pacific results in a front in the SST diurnal cycle.

Getting to the foundation

By definition, T_{fdn} is the temperature of the water below the diurnal warm layer. Thus, near-surface SSTs within the diurnal warm layer, such as the 0.6 m SST measured by Saildrone, Inc. USVs during a mission to the eastern (~125° W) tropical Pacific (Fig. 2a,b), show daytime warming with peak values in late afternoon and a minimum SST at dawn (Fig. 2c). By contrast, the extrapolated T_{fdn} shown in Fig. 2c, computed with the F96 model (Methods and equations (1)–(6)), smoothly tracks dawn SST values. This good agreement with expected characteristics of the foundation SST gives confidence that the model (equation (3)) accurately extrapolates the measured SST to T_{fdn}.

While daytime warming and night-time cooling can lead to large diurnal SST variability at 0.6 m, sharp fronts and eddies can also cause large sub-diurnal variability in SST if the fronts are moving past the fixed observing platform or if the observing platform is moving across the front. In these cases, it is particularly useful to be able to extrapolate the measured SST to a foundation SST to distinguish SST anomalies due to fronts from SST anomalies caused by diurnal warming. As an example, an abrupt front with T_{fdn} change greater than 1 °C in 1 km can be identified in the record on 7 December 2017 near 2° N, 125° W (Fig. 2c, top panel) and on 1 February 2018 near 2° N, 125° W (Fig. 2d and Extended Data Fig. 1).

Extrapolated T_{fdn} is computed for each 10 minute time step from dawn to midnight while the accumulated heat fluxed into the ocean is positive (Methods and equations (3)–(6)). At other times, T_{fdn} is assumed to be the measured SST—an assumption that is reasonable ~dawn but is not as good at midnight (Fig. 2d). The extrapolated T_{fdn} often has a discontinuity at midnight, when the warm-layer model integration ends and the T_{fdn} jumps to the observed bulk SST (Fig. 2d, top panel). This could be caused by biases in the net surface heat flux or wind stress. However, even without errors, terminating the integration at midnight will cause a discontinuity since late-night measured SST can still be within the deepening, weakly stratified warm layer. In these cases, the measured SST at midnight will be warmer than T_{fdn}. The best estimate of T_{fdn} from the measured SST will be at dawn when the diurnal cycle reaches its local minimum.

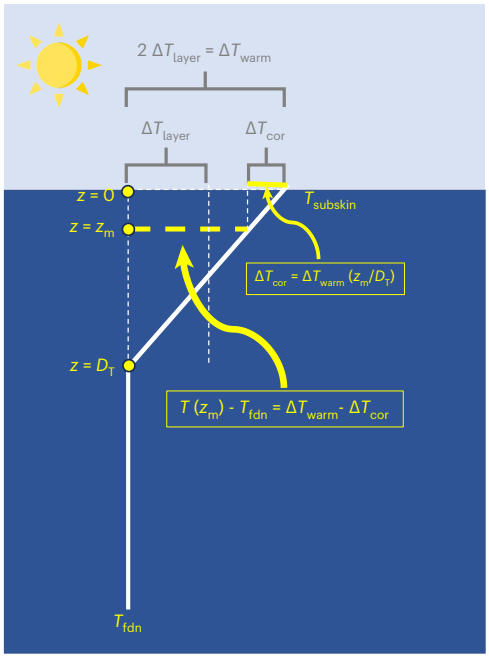

Fig. 1 | Idealized diurnal warm-layer temperature profile[15]. Trapping depth (D_T) is estimated on the basis of the requirement that bulk Richardson number across the warm layer always exceeds a critical value. The warm-layer effect (ΔT_{warm}) is twice the layer-averaged temperature change (ΔT_{layer}), estimated by the surface forcing of a layer of depth D_T. The bulk sea surface temperature $T(z_m)$ is typically measured at a depth of 0.3–2.0 m; it is extrapolated to a subskin temperature $T_{subskin}$ through addition of a temperature correction, ΔT_{cor}, which depends on a proportion of the warm-layer effect. We show that the remaining proportion can be used to extrapolate the bulk temperature to the foundation surface temperature, T_{fdn}. It is assumed that at dawn the diurnal warm layer is fully mixed so that the measured $T(z_m)$ is equivalent to T_{fdn} (Methods). Credit: sun icon, Flaticon.com.

Warm-layer corrections from a 24 hour integration

The midnight discontinuity can be avoided by integrating the diurnal warm-layer model for 24 hours to estimate 24 hour averaged SST warming relative to T_{fdn} (Fig. 2d). Critically, this daily averaged diurnal warm-layer effect can be estimated from daily averaged fluxes if a parameterized gustiness is included in the daily averaged wind stress (Methods and equations (7)–(9)). The gustiness component accounts for the difference between daily averaged scalar wind-stress magnitude and daily averaged wind-stress vector magnitude and ensures that the daily averaged wind-stress values used to force the warm-layer model are non-zero (Extended Data Fig. 2). Inclusion of a stochastic gustiness has been shown to help performance of surface ocean mixed-layer models forced with daily averaged winds[28] and with 3 hour averaged fluxes[9]. Likewise, the COARE bulk-flux algorithms[21–23] add a gustiness component to 10 minute and hourly averaged winds to account for missing wind variance at convective timescales. The extrapolated T_{fdn} based on daily averages matches the predawn SST (Fig. 2d, second panel), and the daily averaged temperature effects estimated from 10 minute and daily averaged fluxes (Fig. 2d, third panel) agree well with mean and RMS differences of, respectively, 0.009 °C and 0.04 °C. These, together with the agreement between the daily averaged temperature effect at 0.6 m and the envelope of diurnal high-passed variability (Fig. 2d, bottom panel), all give confidence that satellite-based daily fluxes can be used to explore patterns in the diurnal warming, such as the reduced SST diurnal cycle amplitude observed as the USV crosses the large-scale front from ~7° N to ~2° N (last two weeks of November 2017 in Fig. 2c).

https://doi.org/10.1038/s41561-024-01391-8

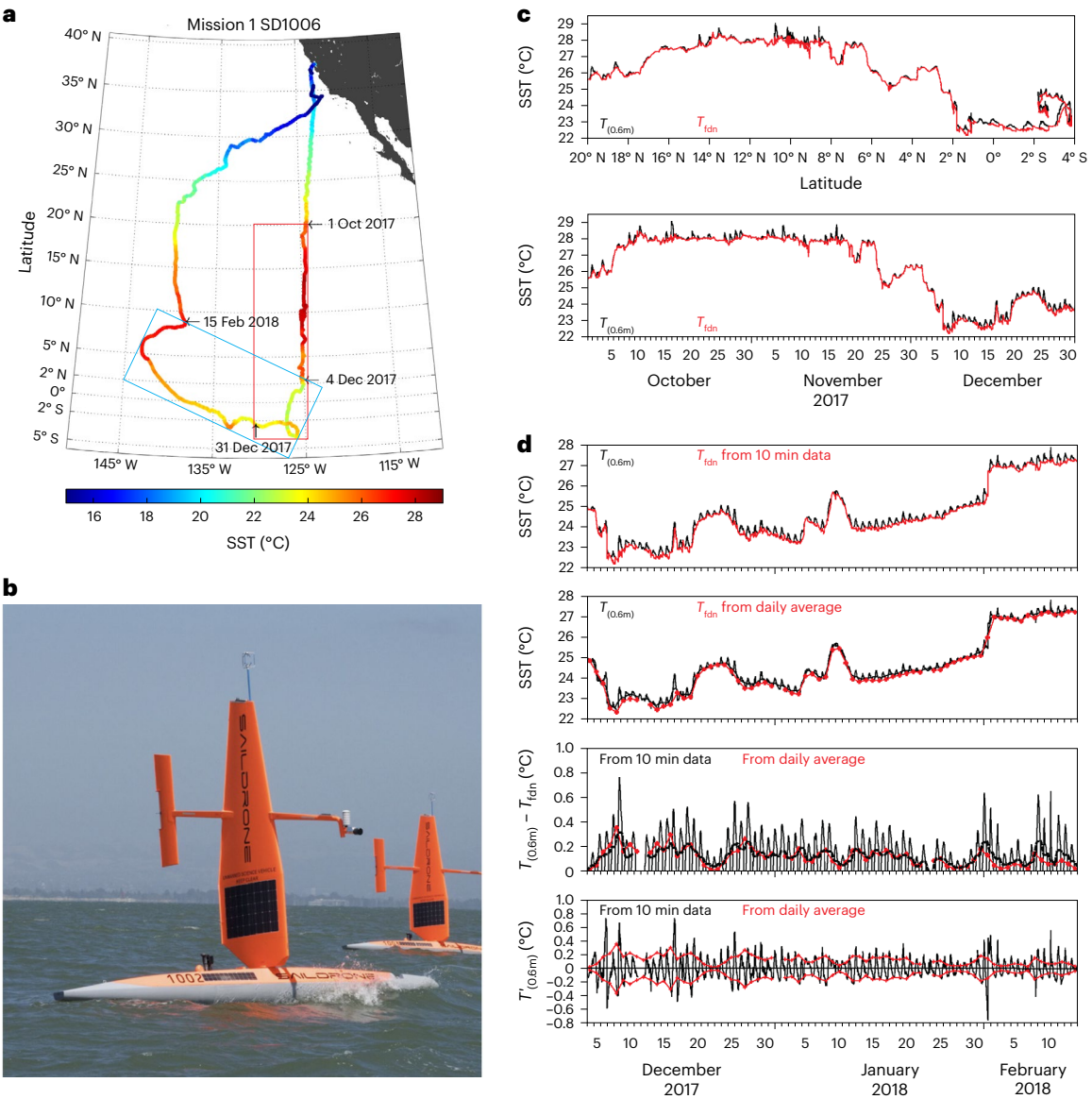

Fig. 2 | TPOS 2017 mission Saildrone #1006 collage. a, Saildrone #1006 (SD1006) track, coloured by SST measured at 0.6 m. **b**, TPOS Saildrone. **c**, Measured SST (black) and extrapolated foundation temperature (T_{fdn}) (red) for the period 1 October 2017 to 1 January 2018, when the drone was south of 20.23° N plotted as a latitude section along ~125° W (upper panel) and time series (lower panel). **d**, SST at 0.6 m (black) and extrapolated T_{fdn} (red) from 10 minute data (top panel) and from daily averaged data with 24 hour running-averaged SST shown in black (second panel). The third panel shows the difference between the SST at 0.6 m and T_{fdn} computed from 10 minute data (black solid), its 24 hour running average (black dashed) and that computed from daily averaged data (red). The bottom panel shows the daily high-passed SST at 0.6 m (black) and plus and minus values of the diurnal warm-layer effect at 0.6 m estimated from daily averaged data (red). Saildrone measurements and flux time series used in the T_{fdn} estimate are shown in Extended Data Figs. 1 and 2. Credit: **b**, Saildrone, Inc.

Effect of SST front on other boundary-layer fronts

With the more complete satellite-based flux fields now available[29], we reproduce the wind and SST patterns for the same day (3 September 1999) as the seminal study[1] in Extended Data Fig. 3 and 6 months later in Extended Data Fig. 4. We see that, indeed, turbulent sensible and latent heat fluxes have a cuspy TIW pattern similar to SST, with near-zero turbulent heat fluxes into the cool eastern equatorial Pacific 'cold tongue' water and large positive values (warming the atmosphere) to the north in the frontal region (Extended Data Fig. 3). These positive turbulent heat fluxes in the frontal region tend to both cool and destabilize the surface oceanic boundary layer (OBL) and warm and destabilize the surface atmospheric boundary layer (ABL). Consequently, as was hypothesized[1], the SST front acts as a front in the atmospheric Monin–Obukhov stability length scale (Methods), L_{atm}, with positive and small values (indicating surface stabilization of the ABL) over the equatorial cold tongue and negative values (indicating destabilization) over the warmer frontal region (Fig. 3a,b). As expected on the basis of stability physics, weaker surface winds are found where the ABL is stabilized, and higher winds are found where the ABL is destabilized. Because heat is removed from the ocean and the OBL is destabilized, no SST diurnal warm layer forms in this frontal region (Fig. 3c and Extended Data Figs. 3 and 4).

In the equatorial Pacific cold tongue, net turbulent heat fluxes, combined with enhanced radiative heat fluxes, produce a very strong net surface heat flux into the ocean. This buoyancy flux, together with the weak winds associated with the weakly stratified ABL there, strongly stabilize the equatorial cold tongue's OBL, as indicated by small and positive oceanic Monin–Obukhov stability length scales, L_{oc} (Fig. 3b

https://doi.org/10.1038/s41561-024-01391-8

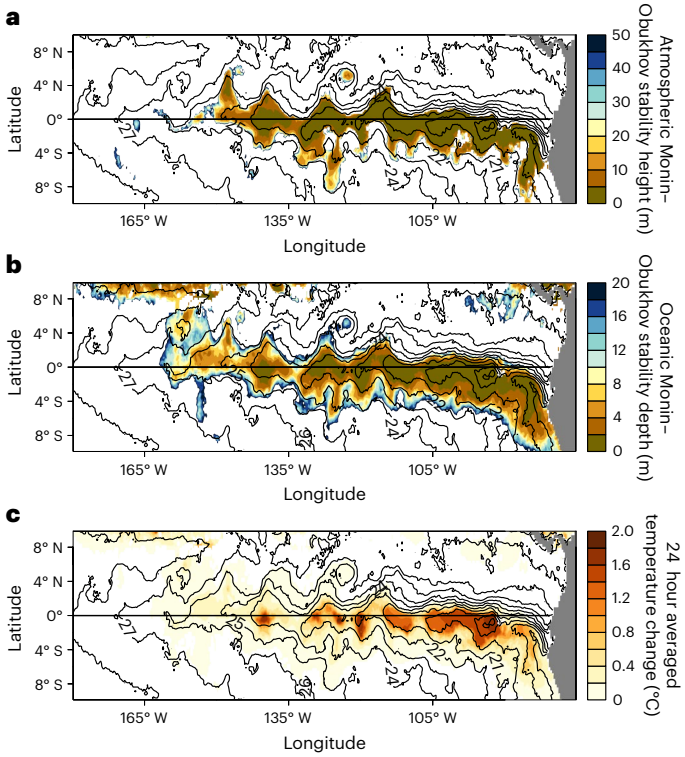

Fig. 3 | J-OFURO3 satellite-based fields for 3 September 1999. a, Small positive atmospheric Monin–Obukhov stability height scales, indicating regions of stabilized ABL, in metres. **b**, Small positive oceanic Monin–Obukhov stability depth scales, indicating regions of stabilized OBLs, in metres. **c**, The 24 hour averaged temperature change in °C due to diurnal warming. SST contours with 1 °C contour intervals are overlaid on all panels. All fields are based on daily J-OFURO3 (ref. 29) fields (Methods).

and Extended Data Fig. 3). Not surprisingly, large SST diurnal warming is observed in the cold-tongue region, with daily average values of ~0.8 °C near 0°, 125° W (Fig. 3c) for 3 September 1999. Furthermore, TIW cuspy patterns in the SST front are evident not only in the ABL and OBL stability fronts, but also in the front of the sea surface diurnal warming (Fig. 3c).

Six months later (Extended Data Fig. 4), when the equatorial cold tongue is less well defined, destabilizing turbulent heat fluxes (out of the ocean) are found throughout most of the eastern tropical Pacific, and positive and small L_{atm} (indicating ABL stabilization) is found only over the coolest equatorial and coastal waters. In general, regardless of season, when there is surface stabilization of the ABL, there tends to be surface stabilization of the OBL. However, the correlation between L_{atm} and L_{oc} is not perfect: a stabilizing L_{oc} is not always associated with a stabilizing L_{atm} due to the different radiation absorption properties of water and air. Surface radiative fluxes directly affect buoyancy within the OBL but not within the ABL. Thus, ABL and OBL stability length scales are most correlated in cloudy regions, such as in the stratus deck of the coastal upwelling zones, the stratocumulus region of the equatorial cold tongue and the deep convective cumulus regions associated with the intertropical tropical convergence zones (Fig. 3a,b and Extended Data Fig. 3).

Seasonal modulation of the diurnal variations

The Tropical Pacific Observing System (TPOS) mooring array, used for monitoring and predicting El Niño/Southern Oscillation, has been observing hourly or better 1 m SST, thermocline depth and surface meteorology for over 20 years[30], enabling analysis of diurnal cycle patterns in both the ocean and atmosphere. In addition, select sites have been enhanced to measure air–sea fluxes and barometric pressure, either as part of a process study[31,32] or as part of the OceanSITES network of sustained observations[33]. Seasonal climatologies of ABL stability, indicated by the air–sea temperature difference (Fig. 4), exhibit large variability spatially and over timescales from diurnal and seasonal to the mean. At all sites, with the exception of the eastern and central equatorial Pacific, the ABL is unstable (surface air temperature is cooler than SST) throughout the entire seasonal cycle. The largest unstable air–sea temperature difference is found at 2° N in the eastern Pacific and is probably due to the strong SST front there. While the SST diurnal cycle at 0°, 95° W is relatively large throughout the annual cycle (lower right panel of Fig. 4), at 2° N, 95° W, the SST diurnal cycle is large only during the warm SST season when the SST front is weak.

As previously found[34], the wind-speed diurnal cycle (Extended Data Figs. 5 and 6) is largest where the equatorial cold tongue and its front are most pronounced. The phasing of the meridional wind-speed diurnal cycle at 0°, 95° W (Fig. 5 and Extended Data Fig. 5) is somewhat similar to that found over land. This could suggest surface cooling at night-time causes enhanced stability that shields the surface from higher winds aloft, and warm daytime surface temperatures result in enhanced turbulent mixing that carries high winds to the surface[35]. Careful inspection, however, shows that other processes besides stability are at play. For one, as previously noted[34], during August–November when the meridional wind diurnal cycle is largest at 0°, 95° W (Extended Data Fig. 6), night-time ABL is more, not less, unstable, compared with other months (T_{air} less than SST; Fig. 4).

Moored barometric pressure time series at 0°, 95° W and 2° N, 95° W (Fig. 5b,c) show that while the semi-diurnal cycle in barometric pressure dominates at each of these sites, the diurnal cycle dominates in the meridional pressure gradient and is roughly of the correct magnitude (although 25% too large) and phasing to account for the diurnal pulsing in the surface meridional winds, as previously speculated[34]. If the diurnal pulsing of the SST front (Fig. 5a and Extended Data Fig. 7) was fully responsible for these diurnal pressure variations and resulting surface meridional wind pulsing, the barometric pressure sensitivity to SST variations would need to be roughly −0.4 hPa K^{-1}, which is over three times larger than the pressure gradient response to SST front variations associated with TIW[31]. This large apparent sensitivity suggests that other correlated processes might also be at play, such as differential heating of the troposphere across a mean cloudiness and moisture front[36].

Conclusion

There is growing recognition that accurate estimation of air–sea exchanges of heat, moisture, momentum and gases depend on proper representation of the ocean's skin temperature, which is generally cooler but can occasionally be warmer than the bulk SST measured by in situ sensors[8,9,24–26]. When computing air–sea fluxes with the COARE bulk-flux algorithm, measured SST is extrapolated to the surface using a cool-skin correction and a warm-layer correction estimated from a simple one-dimensional mixed-layer model[24] (Fig. 1). In this Article, we show that the F96 warm-layer model can be used to also extrapolate SST to a foundation SST below the diurnal warm layer. Furthermore, using independent observations from the TPOS, including from satellites, buoys and USV, we show that the F96 model integrated for 24 hours can be used to estimate the daily averaged warm-layer effect from daily averaged fluxes if a parameterized gustiness is added to the daily averaged wind stress. This gustiness component is equivalent to the sub-diurnal relative wind-speed variance, or equivalently to the difference between the daily averaged wind-stress magnitude and the magnitude of the daily averaged wind-stress vector (Extended Data Fig. 8). We use a simple parameterization of the sub-diurnal gustiness variance that is based on SST[37] (Methods) since gustiness will be largest in unstable ABL conditions and the ABL's stability is correlated with SST (Fig. 3). We also set a minimum value for wind stress, below which we assume gustiness prevails (Extended Data Fig. 8). Developing and

https://doi.org/10.1038/s41561-024-01391-8

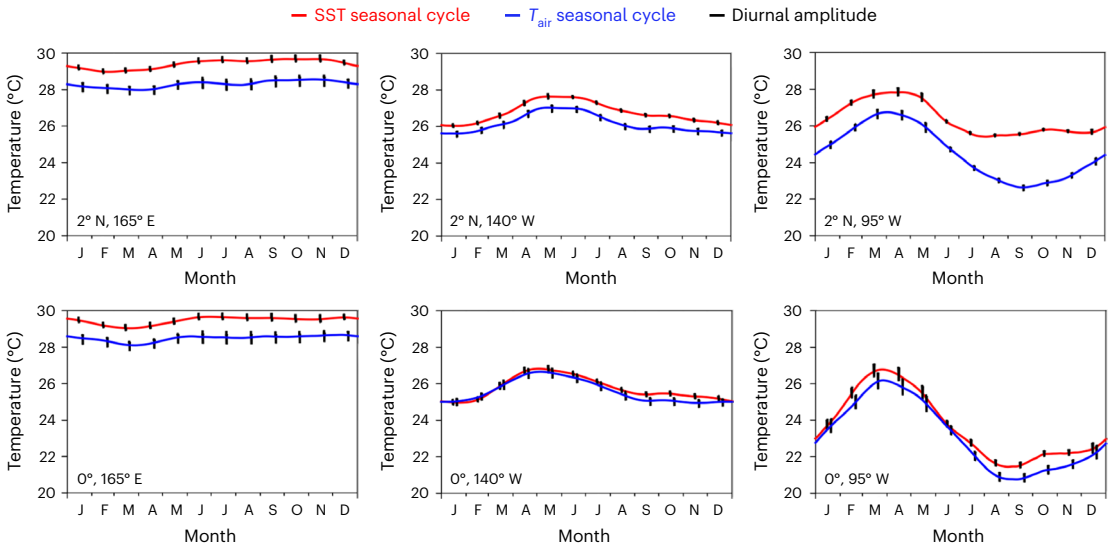

Fig. 4 | SST and air temperature seasonal cycles and diurnal amplitudes for select sites in the TPOS. Range of the diurnal cycle monthly climatologies (black) are overlaid on the monthly 1 m SST climatology (red) and 3 m air temperature climatology (blue).

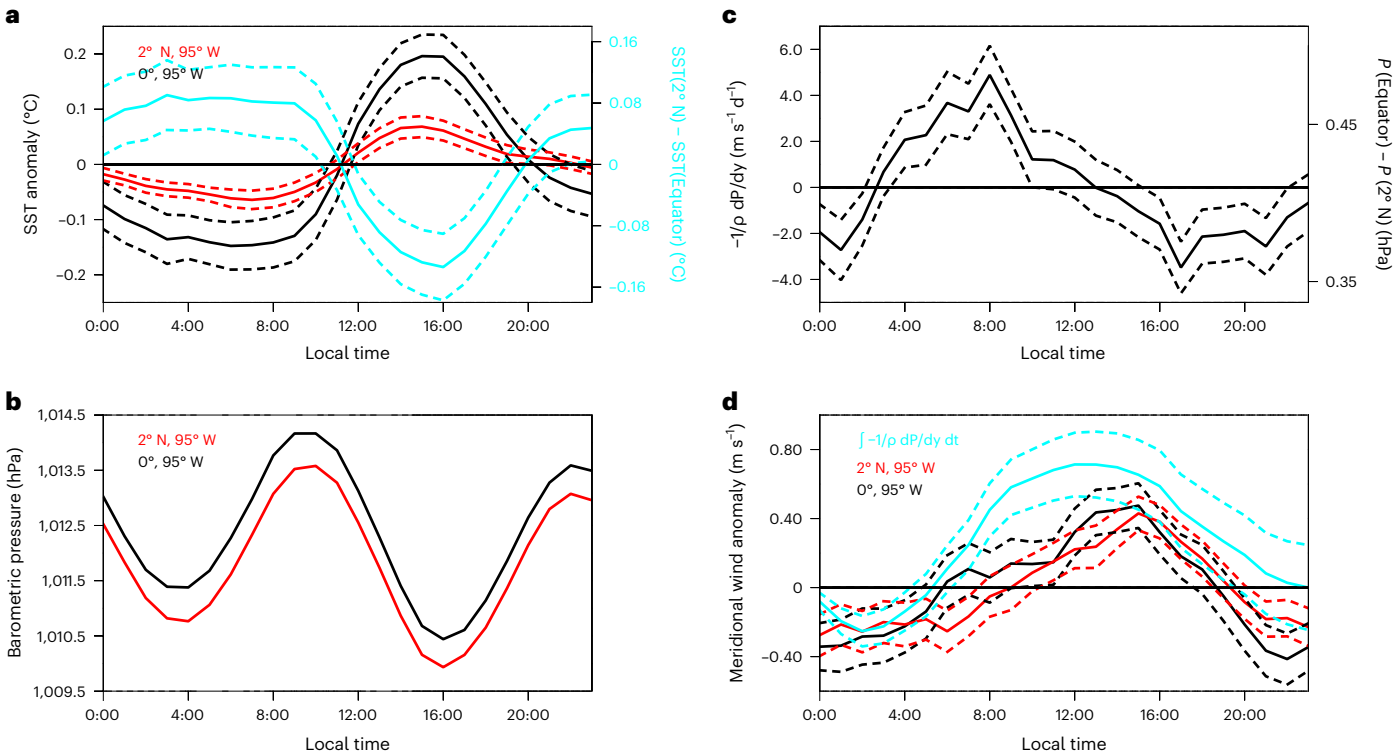

Fig. 5 | 24-hour climatologies for 1 m SST, barometric pressure and meridional winds in the equatorial band at 95° W. a, 1 m SST at 0°, 95° W (black) and 2° N, 95° W (red) and their difference: 2° N minus 0° (light blue; axis on right). **b**, Barometric pressure at 0° N, 95° W (black) and 2°, 95° W (red). **c**, Equator minus 2° N, 95° W barometric pressure difference in units hPa. **d**, Meridional wind anomalies at 0°, 95° W (black), 2°N, 95°W (red), and computed from the pressure gradient anomaly (light blue) in m s^{-1}. All 24 hour climatologies are shown in local time and were computed for the subset of days in the August–November months for the years 2000–2003 when winds, SST and barometric pressure were measured at both sites. In **c**, the corresponding acceleration caused by the pressure gradient anomaly is also shown in units m s^{-1} d^{-1} on the left axis. Standard errors are shown with dashed lines and assume that each day in the composite is an independent degree of freedom.

testing more sophisticated parameterizations of the diurnal gustiness will be the subject of future studies.

Using satellite-based air–sea fluxes[29] to revisit the seminal 3 September 1999 case study[1], it is shown that the eastern equatorial Pacific cold tongue's SST front is also a front in the SST diurnal warming, with a large SST diurnal cycle that rectifies into the daily averaged SST in the equatorial cold tongue. By contrast, SST diurnal cycle is minimal in the warmer frontal regions flanking the equatorial cold tongue. This SST diurnal cycle front represents a front in the OBL and ABL stability length scales, with stabilized OBL and ABL where the SST diurnal cycle is large and destabilized OBL and ABL where the SST diurnal cycle is minimized. We show that the strong diurnal warming

on the cold side of the SST front leads to a diurnal cycle in the strength of the SST front (strongest at dawn and weakest in late afternoon), which appears to lead to a diurnal pulsing of the barometric pressure gradient and meridional surface winds. To the extent that surface heating (as opposed to direct heating of the atmosphere) plays a role in the ABL response to the diurnal (S1) thermal tide, one might expect these SST frontal patterns to modulate not only the diurnal pulsing of the surface branch of the Hadley cell, but also potentially other aspects of the large-scale atmospheric circulation. The novel USVs fill an important gap within the TPOS, providing high temporal- and high spatial-resolution observations over large regions.

The diurnal cycle is a fundamental timescale, representing an external forcing of Earth's system. Daytime near-surface ocean stratification can trap momentum and other properties, leading to rectified impacts on the ocean[10,11,38–40]. Because convective mixing is organized at this timescale, it represents a critical building block process for large-scale convection. By understanding the patterns of the diurnal cycle, we can understand the large-scale patterns stabilizing and destabilizing the OBL and ABL and better understand patterns of convection over the oceans. As such, the diurnal cycle acts as an excellent metric for testing physics of numerical general circulation models.

Online content

Any methods, additional references, Nature Portfolio reporting summaries, source data, extended data, supplementary information, acknowledgements, peer review information; details of author contributions and competing interests; and statements of data and code availability are available at https://doi.org/10.1038/s41561-024-01391-8.

References

1. Chelton, D. B. et al. Observations of coupling between surface wind stress and sea surface temperature in the eastern tropical Pacific. *J. Clim.* **14**, 1479–1498 (2001).
2. Small, R. et al. Air–sea interaction over ocean fronts and eddies. *Dyn. Atmos. Oceans* **45**, 274–319 (2008).
3. O'Neill, L. W., Chelton, D. B. & Esbensen, S. K. The effects of SST-induced surface wind speed and direction gradients on midlatitude surface vorticity and divergence. *J. Clim.* **23**, 255–281 (2010).
4. Samelson, R. M. et al. Surface stress and atmospheric boundary layer response to mesoscale SST structure in coupled simulations of the Northern California Current System. *Mon. Weather Rev.* **148**, 259–287 (2020).
5. Seo, H. et al. Ocean mesoscale and frontal-scale ocean–atmosphere interactions and influence on large-scale climate: a review. *J. Clim.* **36**, 1981–2013 (2023).
6. Wallace, J. M., Mitchell, T. P. & Deser, C. The influence of sea surface temperature on surface wind in the eastern equatorial Pacific: seasonal and interannual variability. *J. Clim.* **2**, 1492–1499 (1989).
7. Lindzen, R. S. & Nigam, S. On the role of sea-surface temperature gradients in forcing low-level winds and convergence in the tropics. *J. Atmos. Sci.* **44**, 2440–2458 (1987).
8. Clayson, C. A. & Bogdanoff, A. S. The effect of diurnal sea surface temperature warming on climatological air–sea fluxes. *J. Clim.* **26**, 2546–2556 (2013).
9. Weihs, R. R. & Bourassa, M. A. Modeled diurnally varying sea surface temperatures and their influence on surface heat fluxes. *J. Geophys. Res. Oceans* **119**, 4101–4123 (2014).
10. Masich, J., Kessler, W. S., Cronin, M. F. & Grissom, K. R. Diurnal cycles of near-surface currents across the tropical Pacific. *J. Geophys. Res.* **126**, e2020JC016982 (2021).
11. Cherian, D. A. et al. Off-equatorial deep-cycle turbulence forced by tropical instability waves in the equatorial Pacific. *J. Phys. Oceanogr.* **51**, 1575–1593 (2021).
12. Kawai, Y. & Wada, A. Diurnal sea surface temperature variation and its impact on the atmosphere and ocean: a review. *J. Oceanogr.* **63**, 721–744 (2007).
13. Yang, B., Emerson, S. R. & Cronin, M. F. Skin temperature correction for calculations of air–sea oxygen flux and annual net community production. *Geophys. Res. Lett.* **49**, e2021GL096103 (2022).
14. Chen, S. S. & Houze, R. A. Jr. Diurnal variation and life-cycle of deep convective systems over the tropical Pacific warm pool. *J. R. Meteorol. Soc.* **123**, 357–388 (1997).
15. Bernie, D. J. et al. Impact of resolving the diurnal cycle in an ocean–atmosphere GCM. Part 2: a diurnally coupled CGCM. *Clim. Dyn.* **31**, 909–925 (2008).
16. Seo, H., Subramanian, A. C., Miller, A. J. & Cavanaugh, N. R. Coupled impacts of the diurnal cycle of sea surface temperature on the Madden–Julian Oscillation. *J. Clim.* **27**, 8422–8443 (2014).
17. Clayson, C. A. & Edson, J. B. Diurnal surface flux variability over western boundary currents. *Geophys. Res. Lett.* **46**, 9174–9182 (2019).
18. Donlon, C. et al. The Global Ocean Data Assimilation Experiment High-Resolution Sea Surface Temperature Pilot Project. *Bull. Am. Meteorol. Soc.* **88**, 1197–1214 (2007).
19. Cronin, M. F. & McPhaden, M. J. Diurnal cycle of rainfall and surface salinity in the western Pacific warm pool. *Geophys. Res. Lett.* **26**, 3465–3467 (1999).
20. Gentemann, C. L., Donlon, C. J., Stuart-Menteth, A. & Wentz, F. J. Diurnal signals in satellite sea surface temperature measurements. *Geophys. Res. Lett.* **30**, 1140 (2003).
21. Fairall, C. W., Bradley, E. F., Rogers, D. P., Edson, J. B. & Young, G. S. Bulk parameterization of air–sea fluxes for Tropical Ocean–Global Atmosphere Coupled Ocean–Atmosphere Response Experiment. *J. Geophys. Res.* **101**, 3747–3764 (1996a).
22. Fairall, C. W., Bradley, E. F., Hare, J., Grachev, A. & Edson, J. Bulk parameterization of air–sea fluxes: updates and verification for the COARE algorithm. *J. Clim.* **16**, 571–591 (2003).
23. Edson, J. B. et al. On the exchange of momentum over the open ocean. *J. Phys. Oceanogr.* **43**, 1589–1610 (2013).
24. Fairall, C. W. et al. Cool-skin and warm-layer effects on sea surface temperature. *J. Geophys. Res.* **101**, 1295–1308 (1996).
25. Donlon, C. J. et al. Toward improved validation of satellite sea surface skin temperature measurements for climate research. *J. Clim.* **15**, 353–369 (2002).
26. Watson, A. J. et al. Revised estimates of ocean–atmosphere CO_2 flux are consistent with ocean carbon inventory. *Nat. Commun.* **11**, 4422 (2020).
27. Wenegrat, J. O. & McPhaden, M. J. Dynamics of the surface layer diurnal cycle in the equatorial Atlantic Ocean (0°, 23°W). *J. Geophys. Res. Oceans* **120**, 563–581 (2015).
28. Giglio, D., Gille, S. T., Subramanian, A. C. & Nguyen, S. The role of wind gusts in upper ocean diurnal variability. *J. Geophys. Res. Oceans* **122**, 7751–7764 (2017).
29. Tomita, H., Hihara, T., Kako, S., Kubota, M. & Kutsuwada, K. An introduction to J-OFURO3, a third-generation Japanese ocean flux data set using remote-sensing observations. *J. Oceanogr.* **75**, 171–194 (2019).
30. McPhaden, M. J. et al. The Tropical Ocean–Global Atmosphere (TOGA) observing system: a decade of progress. *J. Geophys. Res.* **103**, 14169–14240 (1998).
31. Cronin, M. F., Xie, S.-P. & Hashizume, H. Barometric pressure variations associated with eastern Pacific tropical instability waves. *J. Clim.* **16**, 3050–3057 (2003).
32. Cronin, M. F., Fairall, C. W. & McPhaden, M. J. An assessment of buoy-derived and numerical weather prediction surface heat fluxes in the tropical Pacific. *J. Geophys. Res.* **111**, C06038 (2006).

33. Send, U. et al. OceanSITES. In *Proc. OceanObs'09: Sustained Ocean Observations and Information for Society* Vol. 2 (eds Hall, J. et al.) 913–922 (ESA, 2010); https://doi.org/10.5270/OceanObs09.cwp.79
34. Ueyama, R. & Deser, C. A climatology of diurnal and semidiurnal surface wind variations over the tropical Pacific Ocean based on the tropical atmosphere ocean moored buoy array. *J. Clim.* **21**, 593–607 (2008).
35. Thorpe, A. J. & Guymer, T. H. The nocturnal jet. *Q. J. R. Meteorol. Soc.* **103**, 633–653 (1977).
36. Sakazaki, T. & Hamilton, K. Physical processes controlling the tide in the tropical lower atmosphere investigated using a comprehensive numerical model. *J. Atmos. Sci.* **74**, 2467–2487 (2017).
37. Praveen Kumar, B., Vialard, J., Lengaigne, M., Murty, V. S. N. & McPhaden, M. J. TropFlux: air–sea fluxes for the global tropical oceans—description and evaluation. *Clim. Dyn.* **38**, 1521–1543 (2012).
38. Wenegrat, J. O. & McPhaden, M. J. A simple analytical model of the diurnal Ekman layer. *J. Phys. Oceanogr.* **46**, 2877–2894 (2016).
39. Shcherbina, A., D'Asaro, E. A. & Harcourt, R. Rain and sun create slippery layers in the eastern Pacific fresh pool. *Oceanography* **32**, 98–107 (2019).
40. Hughes, K. G., Moum, J. N. & Shroyer, E. L. Evolution of the velocity structure in the diurnal warm layer. *J. Phys. Oceanogr.* **50**, 615–631 (2020).

Methods

Saildrone air–sea flux observations

Saildrones are wind- and solar-powered USVs manufactured and piloted by Saildrone, Inc. Data used here are from drone 1006 during the 2017 TPOS mission[41] to the tropics at 125° W (Fig. 2 and Extended Data Figs. 1 and 2). Measurements include wind speed and direction at 5 m height in Earth coordinates, air temperature and humidity at 2.4 m, barometric pressure at 0.3 m, incoming solar radiation and incoming long-wave radiation, SST at 0.6 m and surface currents at 6 m. Air–sea fluxes were computed from 10 minute averages using the COARE[23] v.3.5 bulk algorithm. Intercomparisons against a moored flux buoy[41] suggest Saildrone net surface heat flux and wind-stress errors are comparable to the flux mooring[42] (10 W m^{-2} and 0.007 N m^{-2}).

Satellite-based air–sea flux observations

Japanese Ocean Flux datasets with Use of Remote Sensing Observations version 3 (J-OFURO3) is a global dataset of air–sea heat, freshwater and momentum fluxes and related parameters (for example, SST) derived from satellite-based observations[29]. The third-generation product is available as daily means on a 0.25° grid for 1988–2017. It should be noted that the nominal depth of the SST in the J-OFURO3 product is ambiguous as it depends on the treatment of SST from multiple products. Its reliance on microwave satellite products, however, suggests that the SST is probably closer to a subskin temperature rather than a foundation temperature. Its net surface heat flux had a mean bias relative to global buoys of −5.8 W m^{-2} (excessive ocean warming)[43].

Climatological diurnal cycles in the tropical Pacific

High-resolution 10 minute SST at 1 m, solar radiation and wind-speed data from National Oceanic and Atmospheric Administration's moored buoy array within the TPOS[25] over the period of 1998–2019 are used to create monthly, seasonal (3 month averaged) composites of the diurnal cycle. Barometric pressure on and off the Equator was available only during a process study[31] from 2000 to 2003, thus limiting the climatological period for variables shown in Fig. 5. When the zenith angle is large (as the Sun rises and sets), the shields on the air temperature sensors are not necessarily effective at blocking beams of sunlight from directly warming the sensor[44,45]. Consequently, while we show the air temperature diurnal peaks in Fig. 4, in this study we do not compute the diurnal cycle in the ABL stability as represented by the SST minus surface air temperature difference.

As a first step towards creating the diurnal cycle composites, the 10 minute data are hourly averaged, filtered with a 3 day high-pass filter, and then binned in 24 hours of the day. The diurnal cycle is calculated by averaging the data in each hourly bin with its uncertainty measured by the standard error with the assumption that each day is an independent degree of freedom. Seasonal climatologies were created by composite analysis of daily data.

SST definitions

SST has a large vertical structure near the air–sea interface[18]. The ocean skin temperature (T_{skin}) felt by the atmosphere is nearly always cooler than the water just a millimetre below the surface[21,25,46,47]. By contrast, solar radiation can penetrate the thermal skin layer, forming a diurnal warm layer when winds and air–sea turbulent heat fluxes are weak. Thus, bulk SST is typically referred to with its measurement depth, that is, 1 m SST. The foundation SST (T_{fdn}) is the SST below the diurnal warm layer. Estimates of T_{skin} from measurements of T_{fdn} require correction for the cool-skin effect with magnitude ΔT_{cool} and a possible adjustment for the warm-layer effect (ΔT_{warm}):

$$T_{skin} = T_{fdn} + \Delta T_{warm} - \Delta T_{cool} \quad (1)$$

F96 warm-layer model for computing foundation temperature

Because skin temperature is a key state variable for air–sea turbulent (latent and sensible) heat fluxes, the COARE bulk-flux algorithm[21–23] includes a cool-skin correction and a warm-layer correction[24] based on a simplified one-dimensional mixed-layer model[48], forced by the air–sea fluxes estimated using the measured bulk SST. Night-time mixing is assumed to cause the bulk SST to be identical to the foundation SST just before dawn. The diurnal warm-layer stratification is also assumed to be uniform above a trapping depth (D_T) so that the ΔT_{warm} is twice the layer-averaged temperature change relative to T_{fdn} measured by the bulk SST just before dawn at ~6:00 LT (Fig. 1). The T_{skin} can then be estimated from a measured bulk SST at depth z_m according to:

$$T_{skin} = T(z_m) + \Delta T_{warm}\frac{z_m}{D_T} - \Delta T_{cool} \quad (2)$$

The second term on the right-hand side of equation (2) is often referred to as the warm-layer correction (for example, Fig. 1), while the third term is the cool-skin correction (typically 0.17 °C) (refs. 25,26).

For computation of the foundation temperature based on the measured bulk SST, equations (1) and (2) can be rearranged according to:

$$T_{fdn} = T(z_m) - \Delta T_{warm} + \Delta T_{warm}\frac{z_m}{D_T} \quad (3)$$

Note that the third term on the right-hand side of equation (3) is the warm-layer correction for skin temperature extrapolations and contributes only if the trapping depth is relatively shallow (not more than twice as deep as the measurement depth). The T_{fdn} in equation (3) can thus be calculated for each time step and saved during runtime of the warm-layer correction of the COARE bulk-flux algorithm[21–23].

The F96 warm-layer model modified for 24 hour integration

Because a linear temperature profile above the trapping depth is assumed, the warm-layer temperature change at the air–sea interface will be double the layer-averaged temperature change, that is, $\Delta T_{warm} = 2\Delta T_{layer}$. As shown in Fig. 1, F96 (ref. 24) estimates the vertically averaged temperature and velocity changes within a layer above a trapping depth, D_T, which is defined as where the surface-forced conditions relative to the foundation temperature reach a critical Richardson number of 0.65. In particular:

$$\Delta T_{layer}(t) = \frac{1}{\rho_{oc}C_{p,oc}D_T}\int_{6LT}^{t}(Q_0 - Q_{pen})\partial t = \frac{\overline{Q_0} - \overline{Q_{pen}}}{\rho_{oc}C_{p,oc}D_T}\int_{6LT}^{t}\partial t \quad (4)$$

$$\Delta u_{layer}(t) = \frac{1}{D_T}\int_{6LT}^{t}u_{*,oc}^2\partial t = \frac{1}{D_T}(\overline{u_{*,oc}}^2 + \overline{gust_{oc}})\int_{6LT}^{t}\partial t \quad (5)$$

$$Ri_{cr} = \frac{g\frac{\partial\rho}{\partial T}\Delta T_{layer}D_T}{2\rho_{oc}\,\Delta u_{layer}^2} = 0.65$$

where ρ_{oc} is surface ocean density, $C_{p,oc}$ is the heat capacity of water, g is gravity, the overbars indicate an average from 6:00 LT to time t, Q_0 is the net surface heat flux into the ocean surface, $u_{*,oc}$ is the oceanic frictional velocity estimated from the wind stress and $\overline{gust_{oc}}$ is the variance ('gustiness') in $u_{*,oc}$ (see the following). Penetrative radiation, Q_{pen}, is estimated from the net solar radiation ($Q_{sw,net}$, that is, incoming minus reflected solar radiation) and an absorption profile, f, evaluated at the trapping depth:

$$Q_{pen}(z = D_T) = Q_{sw,net}f(D_T)$$

$$f = (\,0.004(1 - \exp(-D_T/0.014)) + 0.096(1 - \exp(-D_T/0.36))$$

$$+ [5.77(1 - \exp(-D_T/12.82))]\,)/D_T$$

We list here the full absorption polynomial used in the latest version of the COARE bulk algorithm's warm-layer model[49,50], although typically for the 24 hour integration, only the term within the square brackets is significant.

Using equations (4) and (5) within the Richardson number and defining the thermal expansion coefficient as $\alpha = -(1/\rho_{oc})(\partial\rho/\partial T)$, the trapping depth at time t can then be expressed as:

$$D_T = \left[2Ri_{cr}\rho_{oc}C_{p,oc}\right]^{1/2}\frac{\int_{6LT}^{t}u_{*,oc}^2\partial t}{\left[\alpha g\int_{6LT}^{t}(Q_0 - Q_{pen})\partial t\right]^{1/2}} \quad (6)$$

$$D_T = \left[\frac{2Ri_{cr}\rho_{oc}C_{p,oc}I}{\alpha g\left(\overline{Q_0} - \overline{Q_{pen}}\right)}\right]^{\frac{1}{2}}\left(\overline{u_{*,oc}}^2 + \overline{\mathrm{gust}_{oc}}\right) \quad (7)$$

To ensure that ΔT_{warm} is positive definite, the model integrations in equations (4)–(7) are performed only when heat flux is stabilizing (that is, $\overline{Q_0} > 0$ W m^{-2}). At other periods, it is set to zero and the bulk SST is assumed to be the foundation SST.

Within the COARE bulk algorithm, the F96 diurnal warm-layer model (equations (4)–(6)) evaluates the integral as a summation of the high-resolution (for example, 10 minute) integrand. We note, however, that this is equivalent to its average multiplied by the averaging period in units seconds, as long as a gustiness parameter is added to the averaged frictional velocity or wind stress. Thus, while Fig. 2c shows foundation temperature extrapolations computed at each 10 minute time step, in Figs. 2d and 3, the integration is extended to 24 hours (that is, $I = \int_0^t\partial t = 86{,}400$ seconds, and the overbars indicate daily averages). To estimate $\overline{Q_{pen}}$ initially, an empirical relation for D_T as a function of the Monin–Obukhov depth, L_{oc}, is used in equation (7). A first estimate of the trapping depth is then estimated by equation (7) and used to recompute the Q_{pen}, which then is used to compute the trapping depth according to equation (7).

With the trapping depth then determined, the warm-layer effect can be estimated as:

$$\Delta T_{warm} = A\frac{\left(\overline{Q_0} - \overline{Q_{pen}}\right)^{3/2}}{\left(\overline{u_{*,oc}}^2 + \overline{\mathrm{gust}_{oc}}\right)}, \quad (8)$$

where $A = \left[(2\alpha g I)/((\rho_{oc}C_{p,oc})^3 Ri_{cr})\right]^{1/2}$.

The foundation temperature can then be estimated from the measured bulk temperature from equation (3). As shown in Fig. 2d, this net warming for the 24 hour period, computed from daily averaged fluxes, matches the 24 hour averaged high-resolution warming estimate as well as the envelope of high-passed sub-diurnal variability measured by the 0.6 m thermistor, giving confidence that equation (8) can be used with global daily averaged flux fields to analyse patterns in diurnal warming. Furthermore, the J-OFURO3 product is able to qualitatively reproduce the 1 m SST diurnal cycle measured by the TPOS buoy at 0°, 95° W (Extended Data Fig. 8), with discrepancies probably associated with sampling differences and errors in the satellite-based fluxes. Propagation of errors in equation (8) shows that for a 150 W m^{-2} net heat flux into the ocean trapping layer with 3 m s^{-1} wind speed, a 10 W m^{-2} error would result in a 10% (0.07 °C) error in the warm-layer effect. However, for these low wind-stress conditions, a small 0.007 N m^{-2} error can account for a 62% error in wind stress and a corresponding 62% (0.34 °C) error in the warm-layer effect ΔT_{warm}.

Diurnal gustiness

In the F96 model, a convective gustiness is applied to the wind velocity measurements at each time step of the integration. In our analytical version for the 24 hour integration, a diurnal gustiness must be added to the winds to account for diurnal and sub-diurnal variability in the wind speed and direction. This is particularly important in the equatorial cold-tongue region where winds are very light and currents are strong, without which division by zero led to unrealistically large diurnal warming (>20 °C warming). We therefore use a diurnal wind-speed gustiness formula that depends on SST[37]:

$$\Delta ws = 0.18\,\mathrm{m\,s^{-1}\,^{\circ}C^{-1}}(\mathrm{SST} - 18.1\,^{\circ}\mathrm{C})\ \text{for}\ 23.7\,^{\circ}\mathrm{C} < \mathrm{SST} < 29.8\,^{\circ}\mathrm{C}$$

$$\Delta ws = 1\,\mathrm{m\,s^{-1}}\ \text{for}\ \mathrm{SST} < 23.7\,^{\circ}\mathrm{C}$$

$$\Delta ws = 2.1\,\mathrm{m\,s^{-1}}\ \text{for}\ \mathrm{SST} > 29.8\,^{\circ}\mathrm{C}$$

When this wind-speed gustiness, in units metres per second, is combined with a nominal drag coefficient of 0.001, the frictional velocity gustiness can be estimated as:

$$\overline{\mathrm{gust}_{oc}} = \frac{\rho_a}{\rho_{oc}}\overline{\mathrm{gust}_{at}} = \frac{\rho_a}{\rho_{oc}}0.001\times\Delta ws^2 \quad (9)$$

Finally, to match the minimum wind stress observed in the equatorial cold tongue at 0°, 95° W when computed from winds relative to surface currents, the gustiness was increased so that the daily averaged wind stress enhanced by the atmospheric gustiness ($\overline{\mathrm{gust}_{at}}$) never fell below 0.01 N m^{-2}, roughly equivalent to a wind speed of 2.8 m s^{-1}.

Atmospheric and oceanic stability length scales

Air–sea heat and moisture fluxes that affect the density stratification act as a surface buoyancy flux. The net surface heat flux at the ocean surface (Q_0), including the radiative fluxes at the surface of the ocean, and the net precipitation (P) minus evaporation (E) are included in the oceanic buoyancy flux ($B_{0,oc}$). By contrast, the surface ABL stratification is relatively insensitive to radiative fluxes and precipitation, and thus the atmospheric buoyancy flux ($B_{0,atm}$) depends simply on the surface virtual temperature flux $\overline{w'T_v'}|_0$, which can be related to the sensible (Q_{sen}) and latent (Q_{lat}) heat fluxes according to:

$$B_{0,atm} = \frac{g}{T_v}\overline{w'T_v'}|_0 = \frac{g}{T_v}\left(\frac{Q_{sen}}{\rho_{atm}C_{p,atm}} + 0.61\frac{Q_{lat}}{\rho_{atm}L_e}\right)$$

$$B_{0,oc} = \frac{g}{\rho_{oc}}\overline{w'\rho_{oc}'}|_0 = \frac{g}{\rho_{oc}}\left(\frac{\partial\rho}{\partial T}\frac{Q_0}{\rho_{oc}C_{p,oc}} + \frac{\partial\rho}{\partial S}S(P-E)\right)$$

where g is gravity, S is the salinity of the surface water, T and T_v are water temperature and virtual air temperature, and $C_{p,atm}$ and $C_{p,oc}$ are, respectively, the specific heat of air and water.

The Monin–Obukhov stability scale is the height where the wind-stress production of mechanical turbulent energy balances or is equivalent to the buoyancy flux. The stability scales for the atmospheric (L_{atm}) and oceanic (L_{oc}) boundary layers are computed using, respectively, the atmospheric buoyancy flux ($B_{0,atm}$) and oceanic buoyancy flux ($B_{0,oc}$):

$$L_{atm} = z\left(\overline{u'w'}|_{0,atm}\,\partial u_{atm}/\partial z\right)/B_{0,atm} = u_{*,atm}^3/\left(kB_{0,atm}\right)$$

$$L_{oc} = z\left(\overline{u'w'}|_{0,oc}\,\partial u_{oc}/\partial z\right)/B_{0,oc} = u_{*,oc}^3/\left(kB_{0,oc}\right)$$

where k is the von Karmon constant (taken to be 0.4 for both the atmosphere and ocean, with $\partial u/\partial z \sim u_*/(kz)$). The frictional velocities in the oceanic ($u_{*,oc}$) and atmospheric ($u_{*,atm}$) boundary layers of density ρ_{oc} and ρ_{atm} relate to the wind stress (τ_0) according to:

$$\tau_0 = \rho_{atm}\overline{u'w'}|_{0,atm} = \rho_{atm}\,u_{*,atm}^2 = \rho_{oc}\,u_{*,oc}^2 = \rho_{oc}\overline{u'w'}|_{0,oc}$$

where $\overline{u'w'}|_{0,atm}$ and $\overline{u'w'}|_{0,oc}$ are the co-varying horizontal and vertical turbulent motions in the surface layer of, respectively, the ABL and OBL. Because L_{atm} and L_{oc} in Fig. 3 are estimated with daily averaged

data, the frictional velocities include the gustiness component (equation (9)).

Our sign convention is intended to indicate magnitudes that are positive throughout most of the ocean. Thus, a positive value for net surface heat flux and net solar radiation warm the ocean, while net infrared radiation and turbulent sensible and latent heat fluxes are positive if they cool the ocean:

$$Q_0 = Q_{sw,net} - Q_{lw,net} - Q_{sen} - Q_{lat}$$

Thus, in most parts of the world's ocean where air temperature is cooler than the ocean skin temperature, Q_{sen} would have a positive value, indicating turbulent heat fluxes that warm and destabilize the ABL and cool and destabilize the OBL. Likewise, in regions where the turbulent air–sea heat flux warms the OBL and cools the ABL, the atmospheric and oceanic buoyancy fluxes will tend to stabilize the corresponding boundary layers. The ocean can also be stabilized by the net radiative heat fluxes, while the atmosphere tends to be transparent to the radiative fluxes and therefore the atmospheric buoyancy flux depends only on the turbulent fluxes affecting the virtual temperature.

Data availability

Data from drone 1006 from the 2017 TPOS mission are available at https://www.pmel.noaa.gov/ocs/saildrone/data-access. The J-OFURO3 data were accessed from the University of Hawaii Asian-Pacific Data-Research Center website at http://apdrc.soest.hawaii.edu/dods/public_data/J-OFURO/J-OFURO3_V1.1/daily. The daily TRMM Rainfall (3B42 V7) data were accessed from the University of Hawaii Asian-Pacific Data-Research Center website at https://apdrc.soest.hawaii.edu/dods/public_data/satellite_product/TRMM/TRMM_PR/3B42_daily. TPOS mooring data were accessed from the NOAA/PMEL Global Tropical Moored Buoy Array data display-and-delivery website: https://www.pmel.noaa.gov/tao/drupal/disdel/.

References

41. Zhang, D. et al. Comparing air–sea flux measurements from a new unmanned surface vehicle and proven platforms during the SPURS-2 field campaign. *Oceanography* **32**, 122–133 (2019).
42. Colbo, K. & Weller, R. A. Accuracy of the IMET sensor package in the subtropics. *J. Atmos. Ocean. Technol.* **26**, 1867–1890 (2009).
43. Tomita, H., Kutsuwada, K., Kubota, M. & Hihara, T. Advances in the estimation of global surface net heat flux based on satellite observation: J-OFURO3 V1.1. *Front. Mar. Sci.* **8**, 612361 (2021).
44. De Rovere, F., Zanchettin, D., McPhaden, M. J. & Rubino, A. Assessment of radiative heating errors in the tropical atmospheric ocean array marine air temperature measurements. *Environ. Res. Lett.* **17**, 014040 (2022).
45. Anderson, S. P. & Baumgartner, M. F. Radiative heating errors in naturally ventilated air temperature measurements made from buoys. *J. Atmos. Ocean. Technol.* **15**, 157–173 (1998).
46. Wick, G. A., Emery, W. J., Kantha, L. H. & Schlüssel, P. The behavior of the bulk – skin sea surface temperature difference under varying wind speed and heat flux. *J. Phys. Oceanogr.* **26**, 1969–1988 (1996).
47. Zhang, H., Beggs, H., Ignatov, A. & Babanin, A. V. Nighttime cool skin effect observed from Infrared SST Autonomous Radiometer (ISAR) and depth temperatures. *J. Atmos. Ocean. Technol.* **37**, 33–46 (2020).
48. Price, J. F., Weller, R. A. & Pinkel, R. Diurnal cycling: observations and models of the upper ocean response to diurnal heating, cooling, and wind mixing. *J. Geophys. Res.* **91**, 8411–8427 (1986).
49. Ohlmann, J. C. & Siegel, D. A. Ocean radiant heating. Part II: parameterizing solar radiation transmission through the upper ocean. *J. Phys. Oceanogr.* **30**, 1849–1865 (2000).
50. Wick, G. A., Ohlmann, J. C., Fairall, C. W. & Jessup, A. T. Improved oceanic cool-skin corrections using a refined solar penetration model. *J. Phys. Oceanogr.* **35**, 1986–1996 (2005).

Acknowledgements

This work was supported through funds from NOAA Oceanic and Atmospheric Research (OAR) Climate Programs Office, Climate Observations and Monitoring programme (M.F.C., D.Z.), NOAA OAR Global Ocean Monitoring and Observing (GOMO) programme (M.F.C., D.Z., S.M.W., N.A., Saildrone mission), NOAA Office of Marine and Aviation Operations (OMAO) (M.F.C., D.Z., Saildrone mission) and by the Cooperative Institute for Climate, Ocean, & Ecosystem Studies (CICOES) under NOAA Cooperative Agreement NA20OAR4320271, contribution no. 2023-1276 (D.Z., S.M.W, J.E.J.R.E., N.A.). This is PMEL contribution number 5427.

Author contributions

M.F.C. conceived the study, wrote the original and final draft, and created Figs. 1, 2c,d, 3 and 5 and Extended Data Figs. 1–4 and 8. D.Z. created Fig. 4 and Extended Data Figs. 5–7. S.M.W. created Fig. 2a and assembled Fig. 2. All authors provided edits.

Competing interests

The authors declare no competing interests.

Additional information

Extended data is available for this paper at https://doi.org/10.1038/s41561-024-01391-8.

Supplementary information The online version contains supplementary material available at https://doi.org/10.1038/s41561-024-01391-8.

Correspondence and requests for materials should be addressed to Meghan F. Cronin.

Peer review information *Nature Geoscience* thanks the anonymous reviewers for their contribution to the peer review of this work. Primary Handling Editor: James Super, in collaboration with the *Nature Geoscience* team.

https://doi.org/10.1038/s41561-024-01391-8

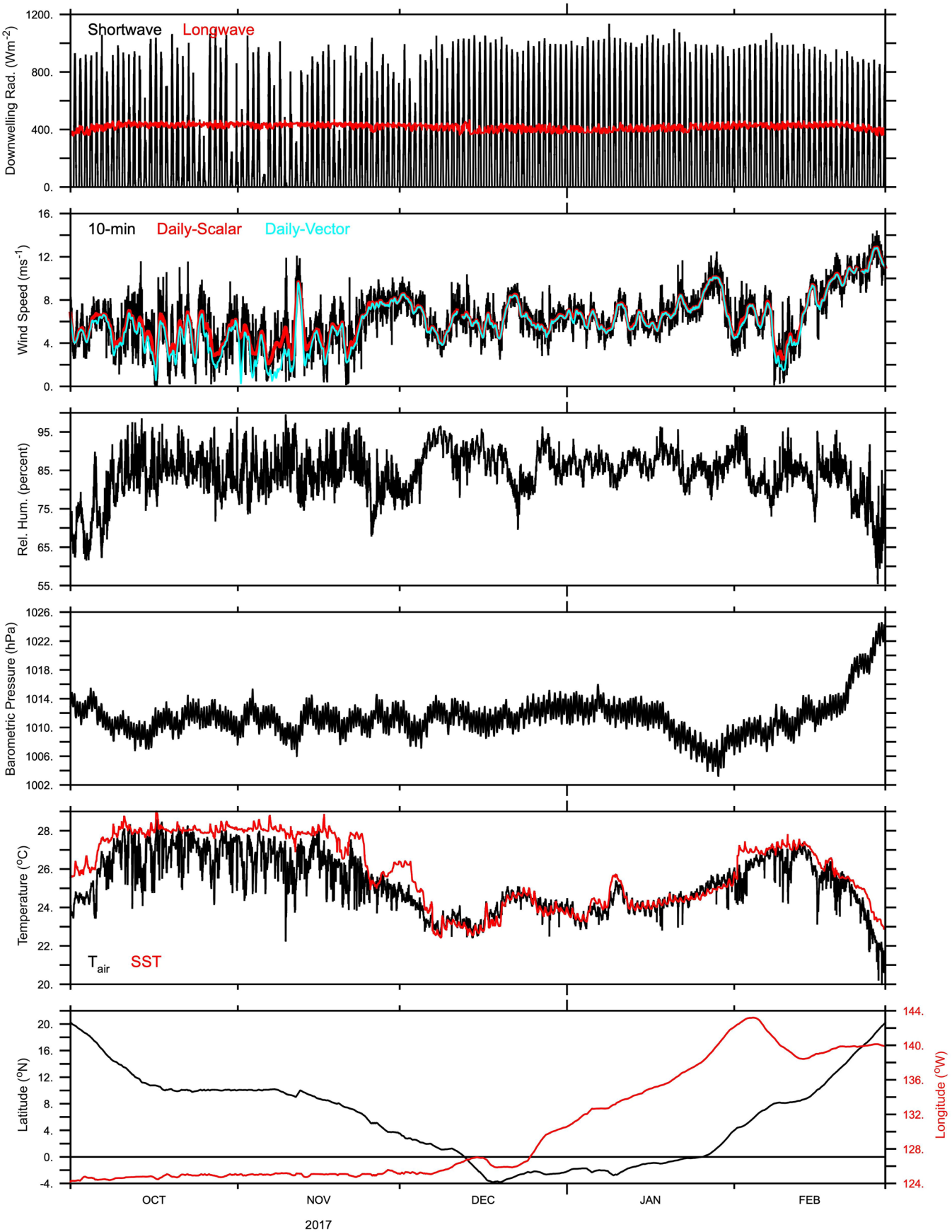

Extended Data Fig. 1 | Ten minute-averaged observations from Drone 1006. From top panel to bottom: Downwelling radiation (shortwave in black, longwave in red) in W m^{-2}, Wind Speed in m s^{-1}, Specific Humidity in g kg^{-1}, Barometric Pressure in hPascals, and air (black) and sea surface (red) temperature in Celsius. For wind speed, the daily averaged time series is overlaid in red and its daily averaged vector wind speed magnitude is in light blue.

https://doi.org/10.1038/s41561-024-01391-8

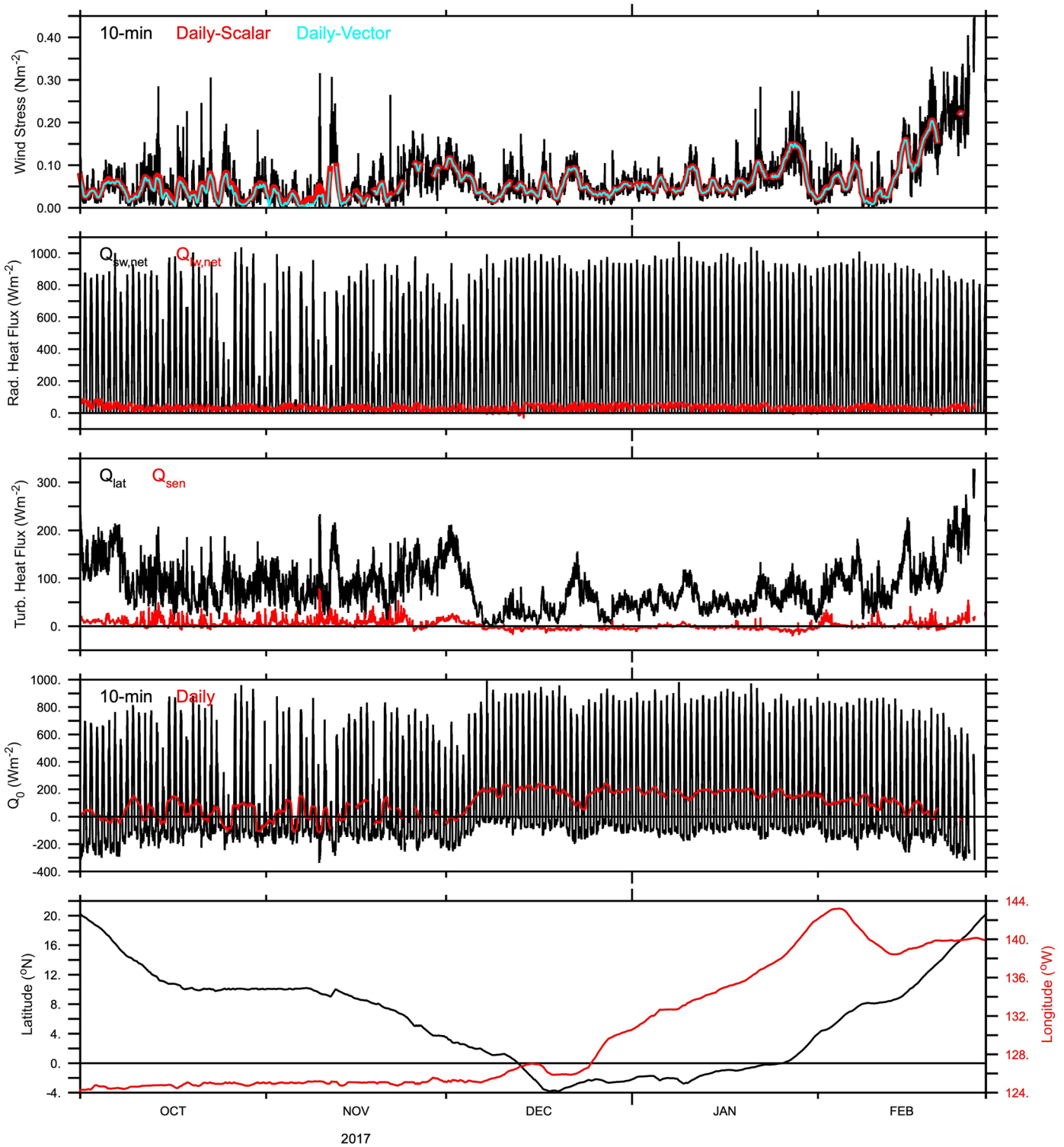

Extended Data Fig. 2 | Ten minute-averaged air-sea fluxes estimated from Drone 1006 observations. From top panel to bottom: Wind stress in N m^{-2}, Net shortwave radiation into sea surface (black) and net longwave radiation out of sea surface (red), Turbulent latent (black) and sensible (red) heat fluxes out of sea surface, and Net surface heat flux into the sea surface. All radiative and turbulent heat fluxes are in W m^{-2}. For wind stress and net surface heat flux, the daily averaged time series is overlaid in red, and the daily averaged vector wind stress (computed from the daily averaged zonal and meridional components) is shown in light blue. The daily averaged scalar can be significantly larger than the vector wind stress when winds are weak and variable.

https://doi.org/10.1038/s41561-024-01391-8

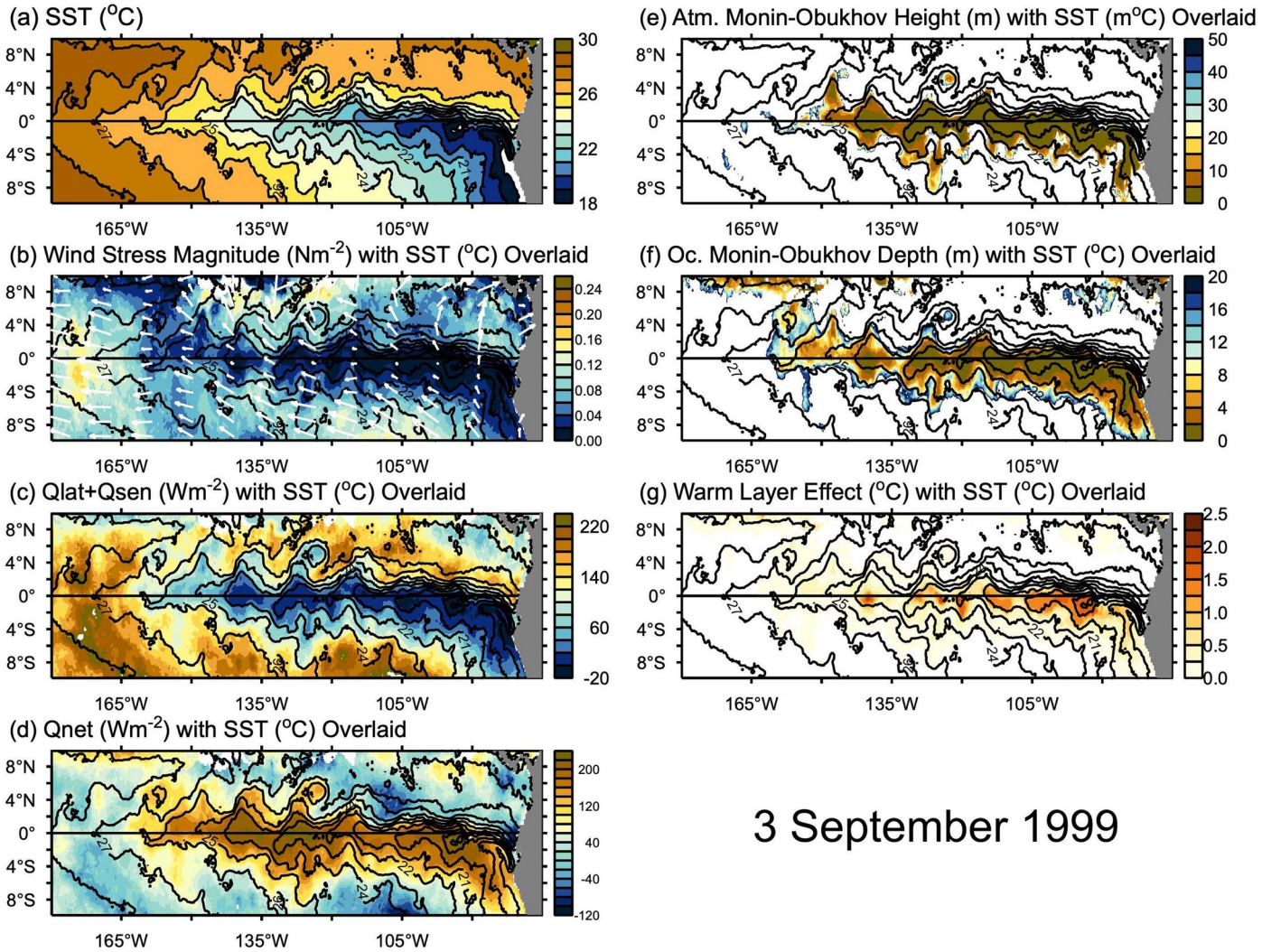

Extended Data Fig. 3 | J-OFURO3 satellite-based fields for September 3, 1999. (**a**) SST in units Celsius, (**b**) wind stress magnitude in units N m^{-2} with surface wind stress vectors, (**c**) surface turbulent heat flux out of the ocean in units W m^{-2}, (**d**) net surface heat flux into the ocean in W m^{-2}, (**e**) small positive atmospheric Monin-Obukhov Stability height scales indicating regions of forced convection within a stabilized atmospheric boundary layer in units meters, and (**f**) small positive oceanic Monin-Obukhov stability depth scales indicating regions of forced convection within stabilized oceanic boundary layers in units meters, (**g**) 24-hour accumulated temperature change in units Celsius due to diurnal warming. SST contours with 1 °C contour intervals are overlaid on all panels. All fields are based upon daily J-OFURO3[26] fields. See METHODS. Note that the convectively active Intertropical Convergence Zone (ITCZ) is located near 7-12°N.

https://doi.org/10.1038/s41561-024-01391-8

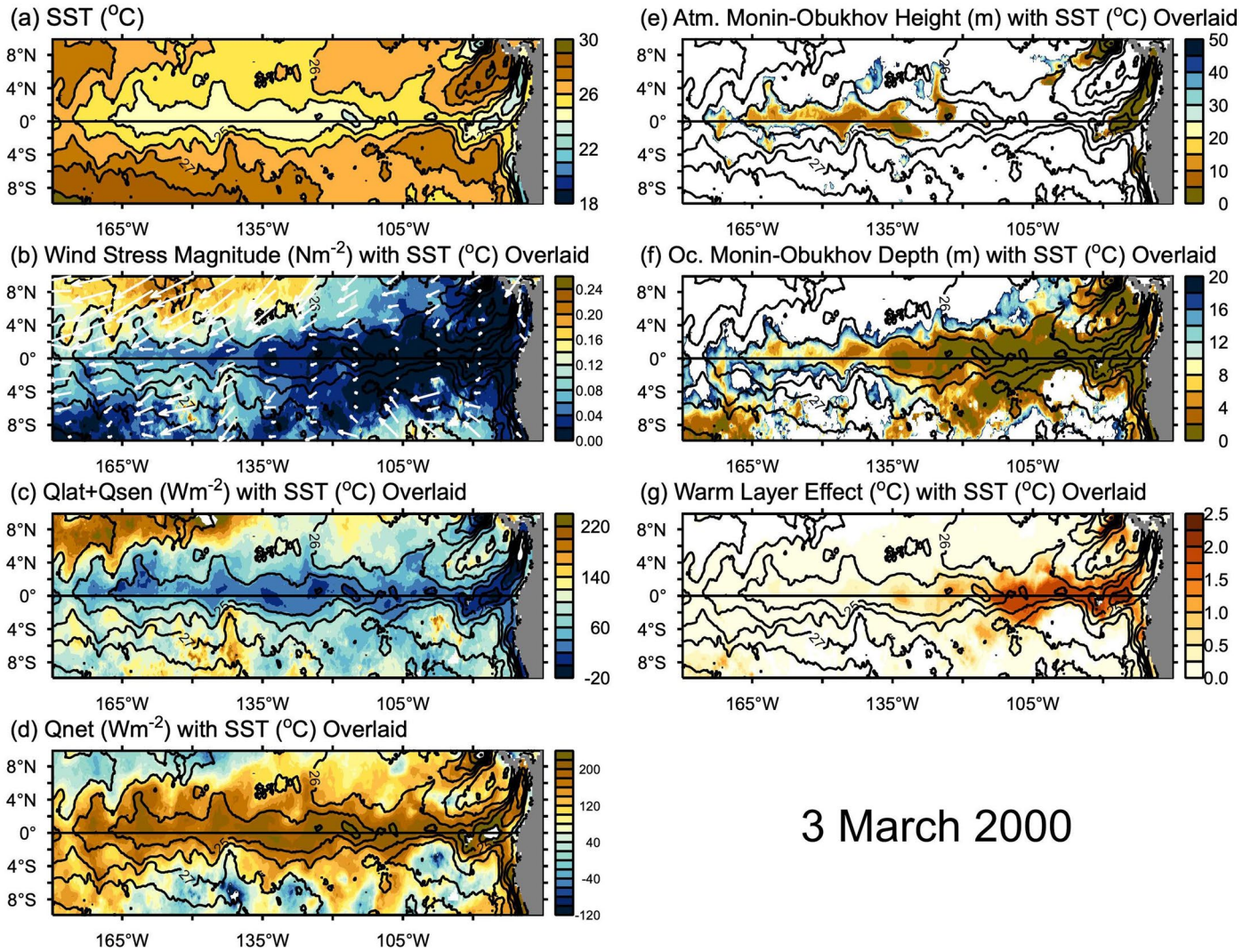

Extended Data Fig. 4 | J-OFURO3 satellite-based fields for March 3, 2000. (a) SST in units Celsius, (b) wind stress magnitude in units N m^{-2} with surface wind stress vectors, (c) surface turbulent heat flux out of the ocean in units W m^{-2}, (d) net surface heat flux into the ocean in W m^{-2}, (e) small positive atmospheric Monin-Obukhov Stability height scales indicating regions of forced convection within a stabilized atmospheric boundary layer in units meters, and (f) small positive oceanic Monin-Obukhov stability depth scales indicating regions of forced convection within stabilized oceanic boundary layers in units meters, (g) 24-hour accumulated temperature change in units Celsius due to diurnal warming. SST contours with 1 °C contour intervals are overlaid on all panels. All fields are based upon daily J-OFURO3 (ref. 26) fields. See Extended Data Fig. 3 for same figure but for September 3, 1999. Note that in March, the Intertropical Convergence Zone (ITCZ) is located close to the equator near 3-5°N. In contrast, as shown in Extended Data Fig. 3, in September the convectively active ITCZ is located near 7-12°N.

https://doi.org/10.1038/s41561-024-01391-8

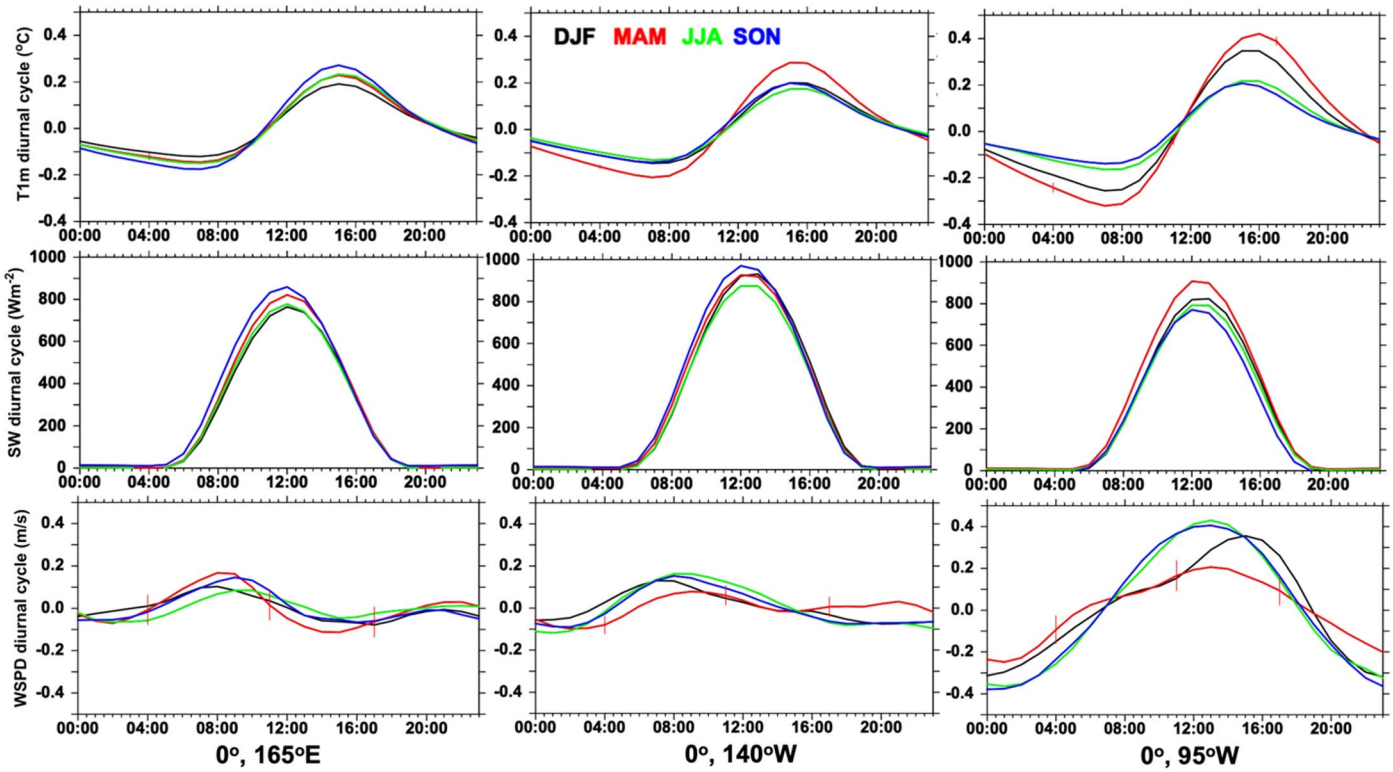

Extended Data Fig. 5 | Diurnal cycle climatologies for SST anomalies, solar radiation, and wind speed anomalies at select sites in the TPOS. Diurnal cycle climatologies for (top row) Sea surface temperature anomalies at 1-m, (middle row) Solar radiation in W m^{-2}, and (bottom row) Wind speed anomaly in m s^{-1}, at three buoy sites: (left) in the western equatorial Pacific at 0°, 165°E; (middle) in the central equatorial Pacific at 0°, 140°W; and (right) in the eastern equatorial Pacific at 0°, 95°W. Different seasons are indicated by colors, with black indicating December-January-February (DJF), red indicating March-April-May (MAM), green indicating June-July-August (JJA), and blue indicating September-October-November (SON). Anomalies are computed relative to a 5-day filter. Standard errors are indicated for the MAM wind speed daily climatologies. See METHODS.

https://doi.org/10.1038/s41561-024-01391-8

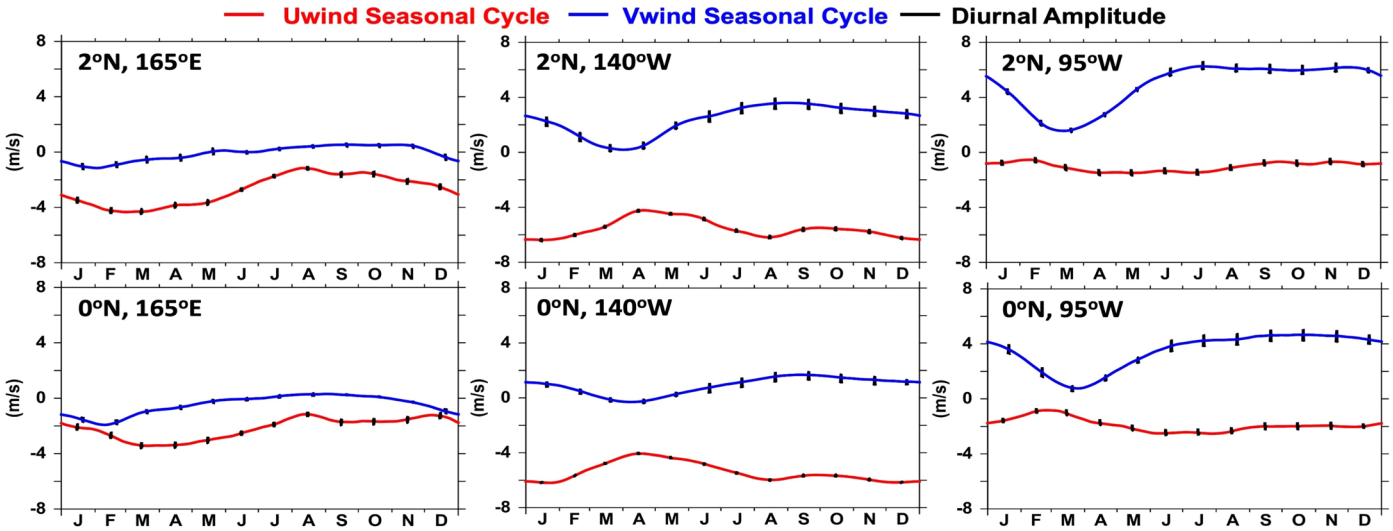

Extended Data Fig. 6 | Monthly climatologies for zonal (red) and meridional (blue) surface 4-meter wind and their diurnal cycle ranges (black) at select sites in the TPOS. Units are m s^{-1}.

https://doi.org/10.1038/s41561-024-01391-8

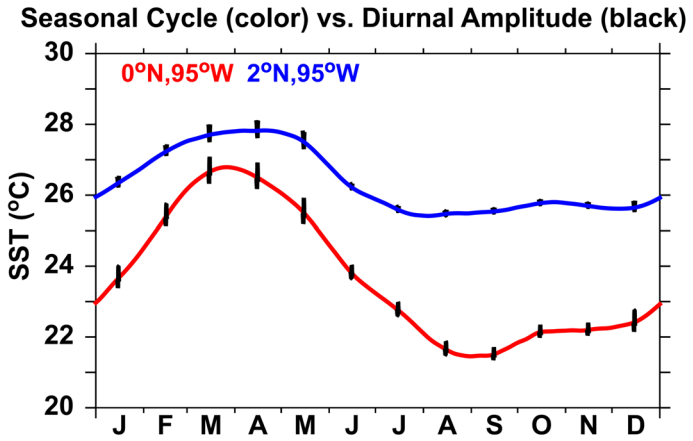

Extended Data Fig. 7 | Diurnal cycle enhancement of the SST meridional gradient along 95°W. Range of the diurnal cycle monthly climatologies in black overlaid on the monthly SST seasonal cycle at 0°, 95°W (red) and 2°N, 95°W (blue) in units degrees Celsius, showing the enhanced meridional SST gradient during August - November (ASON) compared to other months.

https://doi.org/10.1038/s41561-024-01391-8

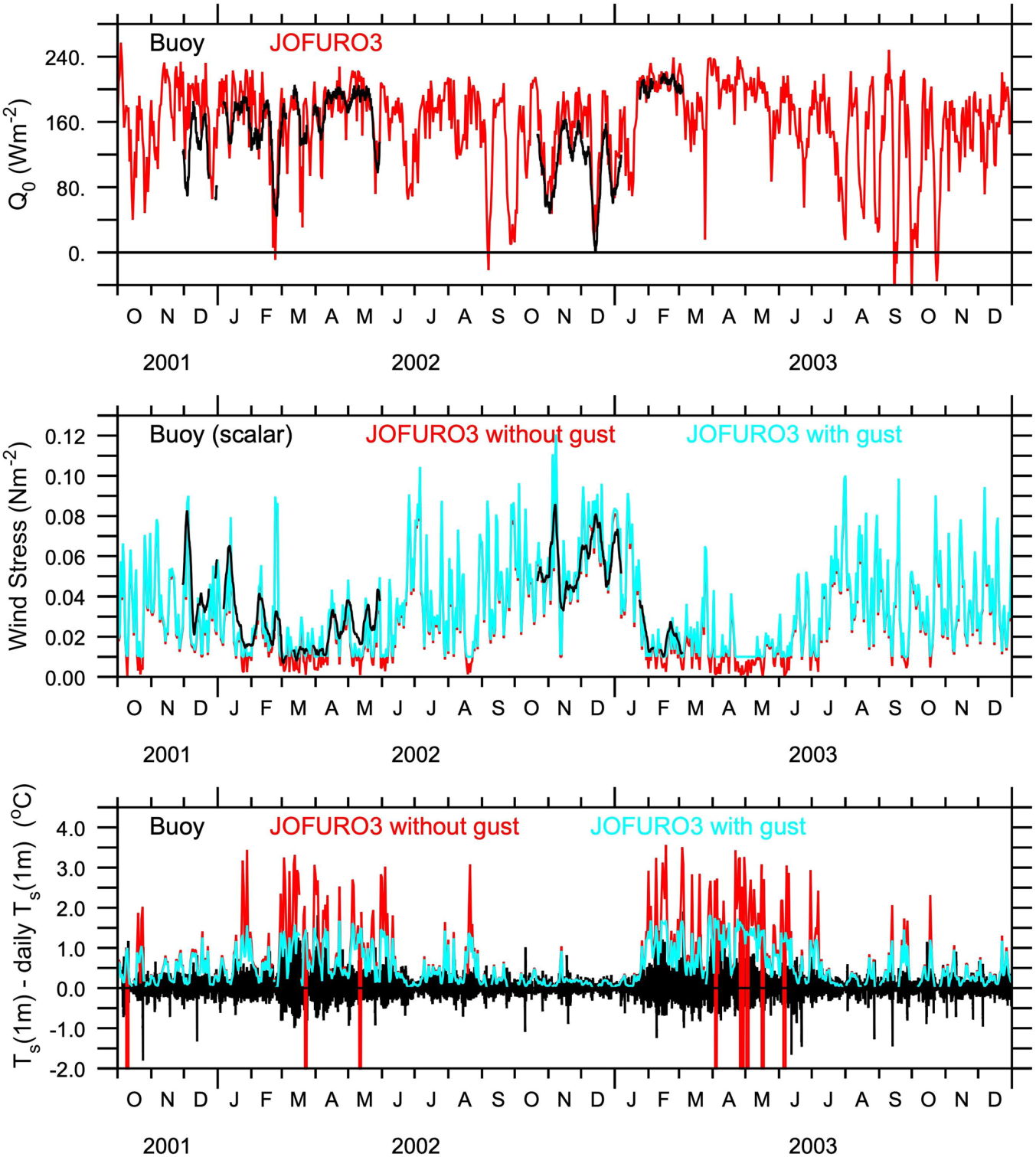

Extended Data Fig. 8 | Intercomparison between a buoy (black) and J-OFURO3 (red) observations at 0°, 95°W. Top panel: Daily-averaged net surface heat flux (Q_0) in units W m^{-2}. Middle panel: Daily-averaged wind stress in units N m^{-2}. The J-OFURO3 daily wind stress without (red) and with (light blue) an additional gustiness included (see METHODS). Bottom panel: Buoy daily high-passed 1-m SST (black) and the average amplitude of the 1-m SST diurnal cycle estimated from J-OFURO3 daily fluxes without (red) and with (light blue) the additional gust. SST values are in degrees Celsius. Note that the buoy's high-passed SST also includes variations due to abrupt fronts. Furthermore, because the positive anomalies are concentrated in the afternoon, while the negative anomalies are spread over nighttime and early morning hours (see Fig. 2d and Extended Data Fig. 5), the average amplitude of the diurnal effect is sometimes less than the positive peak.